ICCFD13-2026-132

A matrix based linear analysis of the numerical shock instability for ideal MHD equations

Y. Shuto* and K. Kitamura*
Corresponding author: shuto-yuta-js@ynu.jp
* Yokohama National University, Japan.

Abstract: We applied the matrix stability analysis of the carbuncle phenomenon to ideal MHD equations for the first time. Perpendicular and parallel shocks are analyzed for Roe, HLL and HLLD schemes. As a result, HLL scheme is always stable in both perpendicular and parallel shocks, while Roe and HLLD schemes are always unstable in parallel shocks, and the stability of them depends on the relationship between upstream Mach number and plasma beta parameter in perpendicular shocks. Moreover, the results suggested the existence of a critical fast magnetosonic Mach number at which the perpendicular shock becomes unstable. Furthermore, we proposed an AUSM-like expression of HLLD scheme and improved the shock robustness by adding the velocity diffusion term into the pressure flux. In particular, the numerical fast magnetosonic speed varying with plasma beta parameter was introduced for the robustness against the parallel shocks. The matrix stability analysis indicated that the present scheme, HLLD+M, improved the stability of both perpendicular and parallel shocks. We confirmed that the present scheme, compared with existing methods such as HLLD, achieved better shock robustness against the carbuncle instability through numerical tests.

Keywords: Carbuncle phenomenon, Shock instability, Stability analysis, Magnetohydrodynamics, Riemann solvers.

1. Introduction

The carbuncle phenomenon is a well-known numerical instability in simulations of compressible flows with shock waves. It was first reported by Peery and Imlay in simulations of blunt body flows with Roe scheme [1]. It typically appears when a strong shock is aligned with the computational grid, leading to non-physical distortions of the shock front and severe degradation of the numerical solution [2]. This instability is most prominently observed in complete approximate Riemann solvers that resolve all waves, such as Roe-type schemes. Previous studies indicated that the carbuncle phenomenon is closely related to the growth of transverse perturbation modes along the shock front [3]. It was reported that the internal shock structure is responsible for the carbuncle phenomenon by Chauvat et al. [4] and Kitamura et al. [5].

In magnetohydrodynamics (MHD), accurate shock-capturing is of crucial importance in many applications, including space and laboratory plasmas. Compared to neutral fluids, MHD equations involve multiple wave families, such as fast and slow magnetosonic waves and Alfvén waves, which significantly complicate numerical shock structures and stability properties. Carbuncle-like instabilities have also been reported in MHD simulations [6, 7]; however, their underlying mechanisms are not yet fully understood.

A systematic analytical approach to the carbuncle phenomenon in neutral fluids is provided by Dumbser et al [8]. In this method, Euler equations are linearized, and a stability matrix is constructed to analyze the temporal evolution of perturbations. Dumbser et al. applied this method to two-dimensional steady shock problems and demonstrated that specific eigenmodes of the stability matrix become unstable above a critical Mach number. This matrix-based approach enables a quantitative identification of unstable modes and provides a theoretical basis for understanding the origin of the carbuncle phenomenon and for designing appropriate stabilization strategies. Chen et al. [9] applied the matrix-based method to a simple cell-shock-cell system and demonstrated that numerical shock instability is essentially a multidimensional phenomenon. Their analysis revealed that the instability originates from the self-instability of the shock upstream cell and is triggered by inappropriate pressure dissipation in the transverse direction. Based on this mechanism, they proposed a fundamental principle for stabilizing shock-capturing schemes [9, 10].

Among shock-capturing schemes, many shock-robust variants of Advection Upstream Splitting Method (AUSM) -family schemes have been developed due to its simplicity and extensibility (e. g. AUSMDV [11], AUSM+ [12], AUSM+up [13], AUSMPW+ [14], SLAU2 [15], AUSM+M [16], AUSM-2025u/p [17]). AUSM-family schemes decompose the numerical flux into mass flux and pressure flux, allowing selective modification of inappropriate dissipations that trigger the carbuncle instability. This modular structure facilitates the development of numerous AUSM-family schemes with shock robustness and other outstanding features. For instance, AUSM+M [16] has stronger shock robustness against carbuncle instability, better low-speed accuracy and higher resolution of oblique shocks by modifying the pressure diffusion term of mass flux, the velocity diffusion term of pressure flux, and the numerical sound speed from AUSM+. In order to provide this extensibility for Harten-Lax-van Leer (HLL) -family flux, AUSM-like expressions of HLL [18] and HLLC [19] were proposed [20, 21]. Kitamura et al. successfully extended HLLC to all speeds based on this AUSM-like form [21].

In MHD, shock-robust schemes have been also proposed [6, 7, 22, 23]. Multistate Low-dissipation Advection Upstream Splitting Method (MLAU) [22] has the accuracy and robustness of AUSM-family schemes and Alfvén wave resolution of HLLD [24] scheme by separating the numerical flux into mass flux, pressure flux, and magnetic tension flux. Low-dissipation HLLD (LHLLD) [23] is an improved HLLD for all speeds and shock robustness. In LHLLD, the pressure difference term of the entropy wave velocity and the velocity diffusion term of the intermediate total pressure are modified by the same techniques used in MLAU. This enables the all-speed applicability and shock robustness of HLLD by simple modification. However, a systematic analysis of these MHD schemes for carbuncle instability has not been conducted before.

In this study, we will first extend the matrix stability analysis developed for neutral fluids to ideal MHD equations in order to investigate the carbuncle phenomenon in MHD systematically. In particular, we will discuss the dependence of stability on Mach number and the plasma beta parameter β. Second, we will apply the AUSM-like expression of HLL-family scheme to HLLD scheme. This formulation allows us to develop a shock-robust HLLD scheme in the same manner as AUSM-family scheme. Here, we will use the magnetic tension flux of MLAU in our proposed formulation.

The rest of the paper is organized as follows. Section 2 provides governing equations and matrix-based analytical method; In Section 3, we apply the matrix stability analysis to perpendicular and parallel shocks. In Section 4, the results of the matrix stability analysis are validated through numerical simulations. Section 5 presents an AUSM-like expression of HLLD, develops an improved HLLD, and analyzes its performance. Section 6 presents numerical results of various benchmark tests including shock waves and high Mach number flows. Section 7 gives the concluding remarks.

2. Analytical method

2.1 Governing equations and discretization

We consider the two-dimensional ideal MHD equations:

$$\frac{\partial \mathbf{Q}}{\partial t}+\frac{\partial \mathbf{F}}{\partial \mathrm{x}}+\frac{\partial \mathbf{G}}{\partial \mathrm{y}}=0, \tag{1}$$

where the conservative variables and flux vectors are

$$\boldsymbol{Q}=\begin{pmatrix}\rho\\ \rho u\\ \rho v\\ \rho w\\ B_x\\ B_y\\ B_z\\ \rho E\end{pmatrix},\ \boldsymbol{F}=\begin{pmatrix}\rho u\\ \rho u^2+p_T-B_x^2\\ \rho uv-B_xB_y\\ \rho uw-B_xB_z\\ 0\\ uB_y-vB_x\\ uB_z-wB_x\\ u(\rho E+p_T)-B_x(\boldsymbol{u}\cdot\boldsymbol{B})\end{pmatrix},\ \boldsymbol{G}=\begin{pmatrix}\rho v\\ \rho vu-B_yB_x\\ \rho v^2+p_T-B_y^2\\ \rho vw-B_yB_z\\ vB_x-uB_y\\ 0\\ vB_z-wB_y\\ v(\rho E+p_T)-B_y(\boldsymbol{u}\cdot\boldsymbol{B})\end{pmatrix}, \tag{2}$$

where ρ, p_T, E are the density, total pressure and total energy respectively, and $\boldsymbol{u}=(u,v,w)^T$ and $\boldsymbol{B}=(B_x,B_y,B_z)^T$ are the fluid velocity and magnetic field. The total pressure and total energy are

$$p_T=p+\frac{|\boldsymbol{B}|^2}{2},$$
$$E=\frac{p}{(\gamma-1)\rho}+\frac{|\boldsymbol{u}|^2}{2}+\frac{|\boldsymbol{B}|^2}{2\rho},$$

where p is thermal pressure and γ is the specific heat ratio, which is taken as 5/3 in this paper.

Considering a finite volume cell Ω_i and boundary faces S_{ik}, we discretize Eq. (1) as follows:

$$\frac{\mathrm{d}\overline{\mathbf{Q}}_i}{dt}+\frac{\sum_{k=1}^{faces}\overline{\boldsymbol{F}}_{ik}S_{ik}}{\Omega_i}=0, \tag{3}$$

where $\overline{\mathbf{Q}}_i$ is the cell-averaged value and $\overline{\boldsymbol{F}}_{ik}$ is the numerical flux passing through the interface.

2.2 Matrix stability analysis

For the matrix-based linear analysis [8], we assume

$$\overline{\mathbf{Q}}_i=\widehat{\boldsymbol{Q}_i}+\delta\overline{\mathbf{Q}}_i, \tag{4}$$

where $\widehat{\boldsymbol{Q}_i}$ is the steady mean value and $\delta\overline{\mathbf{Q}}_i$ is the small perturbation. Substituting (4) into (3) and linearizing the numerical flux function, we obtain the perturbation evolution of all $q=\mathrm{N}\cdot\mathrm{M}$ cells in the domain consisting of N rows and M columns,

$$\frac{d}{dt}\begin{pmatrix}\delta\overline{\mathbf{Q}}_1\\ \vdots\\ \delta\overline{\mathbf{Q}}_q\end{pmatrix}=\boldsymbol{S}\begin{pmatrix}\delta\overline{\mathbf{Q}}_1\\ \vdots\\ \delta\overline{\mathbf{Q}}_q\end{pmatrix}, \tag{5}$$

where $\boldsymbol{S}$ is the stability matrix. Considering only the evolution of initial perturbations, the solution of the linear system (5) is

$$\begin{pmatrix}\delta\overline{\mathbf{Q}}_1\\ \vdots\\ \delta\overline{\mathbf{Q}}_q\end{pmatrix}=e^{St}\begin{pmatrix}\delta\overline{\mathbf{Q}}_1\\ \vdots\\ \delta\overline{\mathbf{Q}}_q\end{pmatrix}_{t=0} \tag{6}$$

The perturbation remains bounded if the maximum of the real part of the eigenvalue λ of $\boldsymbol{S}$ is negative,

$$\max(\mathrm{Re}(\lambda))\leq 0. \tag{7}$$

The flux Jacobian in $\boldsymbol{S}$ is evaluated numerically using a centered approximation as proposed in [8], in order to handle the non-differentiability of numerical flux functions.

3. Applications of the matrix stability analysis to ideal MHD equations

3.1 Application to the perpendicular shock

We apply the matrix stability analysis to ideal MHD equations. We define a uniform Cartesian grid containing 11×11 cells in the domain, where a thin steady perpendicular shock is located between the 6th and the 7th column. Here, a perpendicular shock is a type of MHD shock waves in which the upstream magnetic field is oriented perpendicular to the shock propagation direction [35] as shown in Fig.1(a). A perpendicular shock is a special case of a fast MHD shock and density, pressure and magnetic

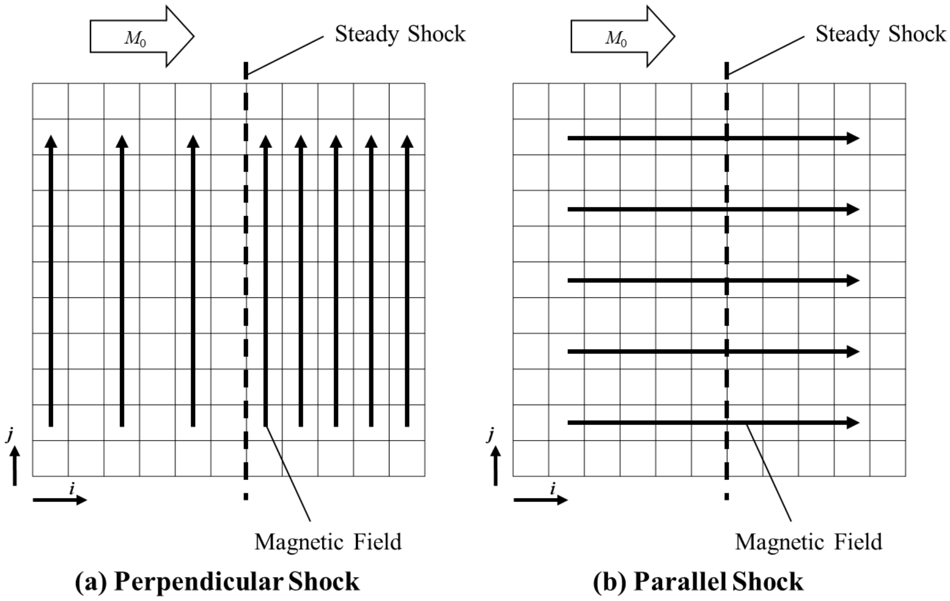

Figure 1: Computational Grid and (a) perpendicular and (b) parallel shock.

field increase across the shock, while the normal component of the magnetic field remains zero. The initial state on the upstream side of the shock is set as follows:

$$\left(\rho_0,\, u_0, v_0, w_0, B_{x0}, B_{y0}, B_{z0},\, p_0\right)^T = \left(1{,}1, 0, 0{,}0, \sqrt{\frac{2}{\gamma {M_0}^2 \beta}}, 0, \frac{1}{\gamma {M_0}^2}\right)^T, \tag{8}$$

where $M_0 = u_0/a_0$ and $\beta = 2p_0/|\boldsymbol{B_0}|^2$ are respectively the upstream thermal sonic Mach number and the upstream plasma beta parameter with the upstream sound speed $a_0 = \sqrt{\gamma p_0/\rho_0}$. Here, we introduce the fast magnetosonic Mach number $M_F = u_0/c_{f0}$ with the upstream fast magnetosonic speed $c_{f0}^2 = a_0^2 + |\boldsymbol{B_0}|^2/\rho_0$. Using the condition $M_F > 1$ in the upstream region of the fast shock, the following relation that M_0 and β must satisfy is derived;

$$\beta > \frac{2}{\gamma\left({M_0}^2 - 1\right)}. \tag{9}$$

The initial state on the downstream side of the shock can be calculated using Rankine-Hugoniot relations for MHD. Random numerical perturbations of the order 10^{-6} are introduced into the entire flow field to trigger instabilities.

The stability of the following schemes has been analyzed: Roe [25], HLL [18] and HLLD [24] which are widely used in MHD simulations. The distributions of the eigenvalues of the stability matrix at $M_0 = 10$ and $\beta = 0.1$ are shown in Fig.2. In this condition, Roe and HLLD schemes are unstable but HLL scheme is stable. The maximum values of the real parts of the eigenvalues against $\beta (0.001 \leq \beta \leq 10$ and Eq. (9)) for each $M_0 (3 \leq M_0 \leq 20)$ are plotted in Fig.3. In Roe and HLLD schemes, for a given

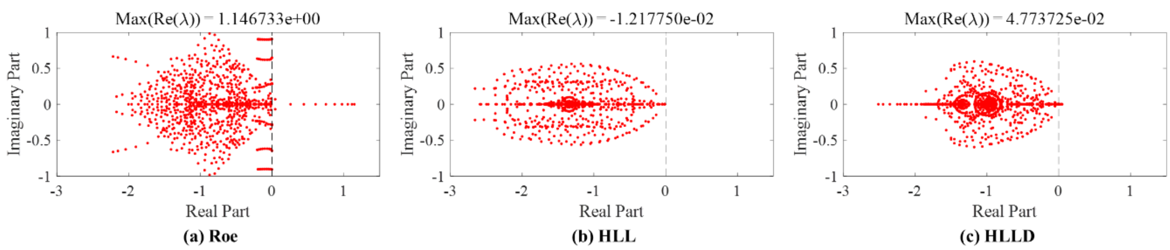

Figure 2: Distributions of the eigenvalues of $\boldsymbol{S}$ in the complex plane at $M_0 = 10$ and $\beta = 0.1$.

M_0, we conducted the analysis while gradually decreasing β. Once the scheme became stable, we moved on the next M_0 and restarted from β in which the scheme became stable at the previous M_0. When M_0 and β are varied, the highly-dissipative HLL scheme always has eigenvalues with negative real parts for $M_0 \leq 20$ and $\beta \leq 10$, while Roe and HLLD schemes have eigenvalues with positive real parts as β becomes larger. It is considered that when the magnetic field is large compared with the gas pressure, the schemes tend to be stable due to the stabilizing effect of the magnetic field [6, 7]. This is likely because in the perpendicular shock, the tangential magnetic field generates the transverse magnetic tension that suppresses transverse perturbations along the shock front, making the shock less susceptible to the carbuncle instability. In addition, Fig.3 shows that Roe scheme has smaller stability thresholds of

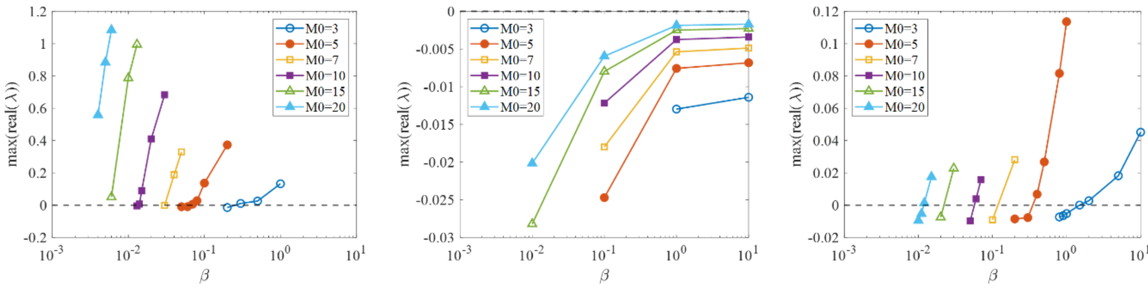

(a) Roe (b) HLL (c) HLLD

Figure 3: Maximum values of the real parts of the eigenvalues against β for each M_0 in perpendicular shocks.

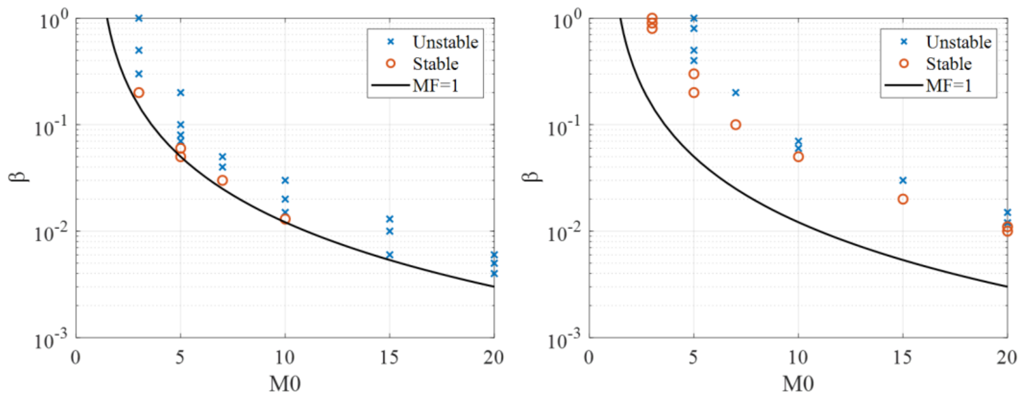

(a) Roe (b) HLLD

Figure 4: Stability maps for M_0 versus β. Circles indicate stable states and crosses indicate unstable states. The curve of $M_F = 1$ represents the lower limit of β.

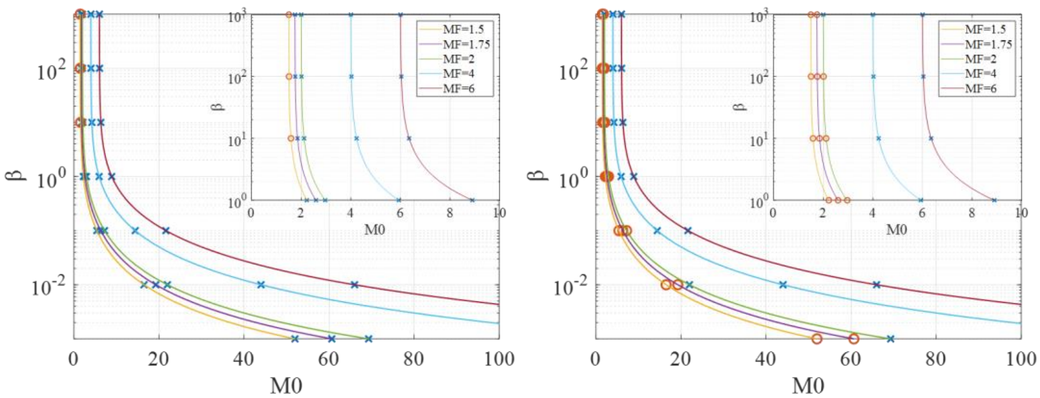

(a) Roe (b) HLLD

Figure 5: Stability maps along the curves obtained from Eq. (10) with M_F as a parameter. The zoomed-in views of the selected regions are shown in the insets.

β than HLLD scheme. This result implies that Roe scheme requires a larger value of magnetic field for stability than HLLD scheme.

Stability maps for the different combinations of M_0 and β are shown in Fig.4. The curve of $M_F = 1$ in Fig.4 represents the lower limit of β given by Eq. (9). Figure 4 suggests that the schemes are more stable in the region closer to the curve of $M_F = 1$. Thus, we hypothesize the existence of a critical value of M_F beyond which the scheme becomes unstable.

In order to clarify the relationship between the stability and M_F, we investigate the stability on the curves where M_F is constant. The curves are expressed by the following equation derived from the relation between M_0, β and M_F:

$$\beta = \frac{2}{\gamma\left(\frac{{M_0}^2}{{M_F}^2} - 1\right)}. \tag{10}$$

The stability maps along the curves obtained from Eq. (10) with M_F as a parameter are presented in Fig.5. The stability is found to be nearly constant along each curve. We can see the schemes are unstable in the regions where M_F is large, whereas the schemes tend to be stable as M_F approaches unity. In particular, when $M_F \leq 1.75$, HLLD is stable regardless of M_0 and β. This result can be regarded as an analogy to the observation that schemes for a neutral fluid become unstable to the shock at high upstream Mach number [8].

3.2 Application to the parallel shock

The stability of a thin steady parallel shock was investigated using the matrix stability analysis. Here, a parallel shock is a type of MHD shock waves in which the magnetic field is parallel to the shock propagation direction [35] as shown in Fig.1(b). The initial state on the Upstream side of the shock is set as follows:

$$\left(\rho_0,\ u_0, v_0, w_0, B_{x0}, B_{y0}, B_{z0},\ p_0\right)^T = \left(1,1,0,0, \sqrt{\frac{2}{\gamma {M_0}^2 \beta}}, 0, 0,\ \frac{1}{\gamma {M_0}^2}\right)^T. \tag{11}$$

Because the magnetic field normal to the shock front does not contribute to the pressure jump across the shock, the jump conditions reduce to those of a hydrodynamic shock. Thus, the initial state on the downstream side of the shock can be calculated using Rankine-Hugoniot relations for a hydrodynamic shock and the normal magnetic field is continuous across the shock. The other analysis conditions are the same as those in the perpendicular shock.

The stability of the following schemes has been analyzed: Roe, HLL and HLLD. The maximum values of the real parts of the eigenvalues against $\beta(10^{-3} \leq \beta \leq 10^3)$ for each $M_0(3 \leq M_0 \leq 20)$ are plotted in Fig.6. As in the case of the perpendicular shock, the eigenvalues become smaller as β becomes smaller in all the schemes. Similarly, HLL scheme always has eigenvalues with negative real parts. However, Roe and HLLD schemes are less stable, because they always have eigenvalues with positive real parts. This implies that a parallel shock is more vulnerable to the carbuncle instability than a perpendicular shock due to the absence of transverse magnetic tension along the shock front.

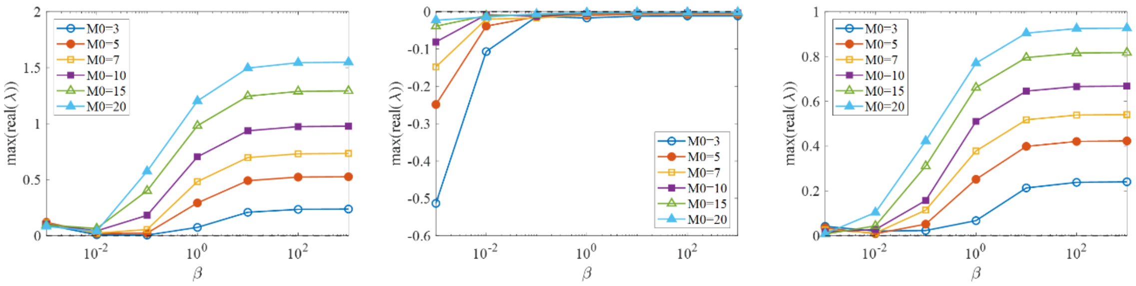

(a) Roe (b) HLL (c) HLLD

Figure 6: Maximum values of the real parts of the eigenvalues against β for each M_0 in parallel shocks.

4. Validation of the matrix stability analysis by numerical experiments

In order to validate the matrix stability analysis for ideal MHD equations, we conducted numerical simulations and compared the numerical results with those of the matrix stability analysis. In the following calculations, we employed 1st-order accuracy in both time and space, and used Roe and HLLD schemes as the numerical flux, where HLL scheme was excluded from the validations since it is always stable. Also, hyperbolic divergence cleaning method [26] was adopted for the numerical treatment to avoid $\nabla \cdot \boldsymbol{B} \neq 0$. The computational grid consists of 25×25 cells and the domain size is 1×1. A thin steady perpendicular/parallel shock is located between the 12th and 13th columns. Random perturbations of the order 10^{-6} are added to the initial values of conservative variables in all cells.

4.1 Validation in the perpendicular shock

The result of the Roe scheme when M_F = 1.5 and 2 at β =100 for the perpendicular shock is shown in Fig.7(a) and (b) as a representative example. Figure 7 indicates that Roe scheme is stable when M_F = 1.5, while it is unstable when M_F = 2 at β = 100, which is consistent with Fig.5. On the other hand, in the HLLD scheme, the carbuncle phenomenon does not occur even under one of the severe conditions that M_F = 6 and β =1 as shown in Fig.7(c). This seems to occur because nonlinear effects become significant after some time from the start of the computation, leading to behavior that deviates from the linear analysis. In Fig.8, we show the evolutions of the maximum values of the transvers velocity for each M_F at β = 0.1 in Roe and β = 1 in HLLD, which represents the numerical error since the exact value should remain zero throughout the computation. Figure 8 indicates that the transverse velocity progresses through an initial transition region, a linear phase and finally a nonlinear saturation stage. Here, the schemes are regarded as unstable when the transverse velocity grows exponentially in the linear phase because the (positive) slope of the exponential growth in a semi-logarithmic plot corresponds to (the maximum value of) the real parts of the eigenvalues in the linear analysis. Based on this criterion, Roe scheme is unstable for all M_F at $\beta = 0.1$, and HLLD scheme becomes unstable for $M_F \geq 4$ at $\beta = 1$, which is consistent with the results shown in Fig.5.We chose this condition because the agreement with the analytical results can be illustrated more clearly, but under some other conditions, slight deviations from the results of the matrix stability analysis are observed with respect to the fast magnetosonic Mach number separating the stable and unstable regimes. This discrepancy can be attributed to the use of centered approximation to evaluate the numerical flux Jacobian when constructing the stability matrix. Nevertheless, the matrix stability analysis is proved to be useful in ideal MHD equations for evaluating the relative stability of numerical schemes.

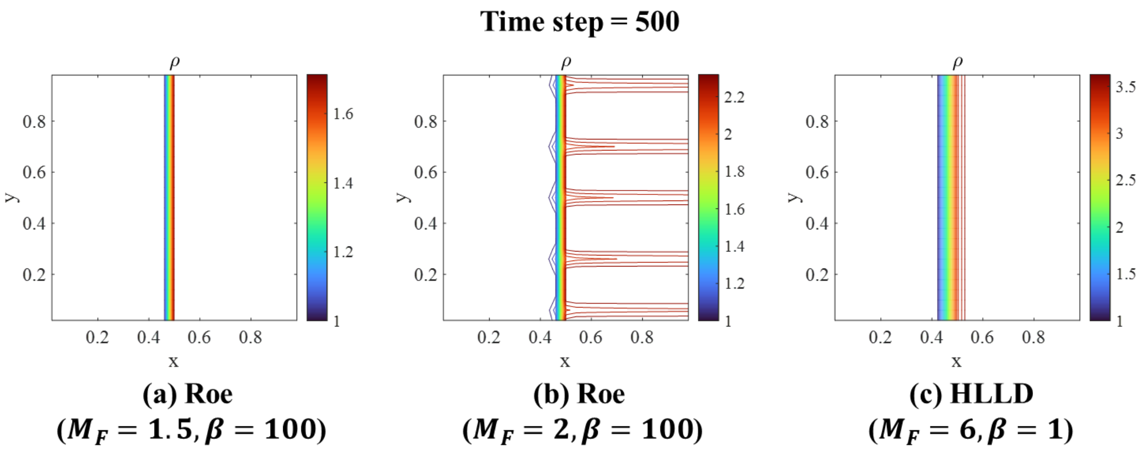

Figure 7: Density contours with Roe and HLLD schemes in perpendicular shocks: (a) stable, (b) unstable, (c) stable.

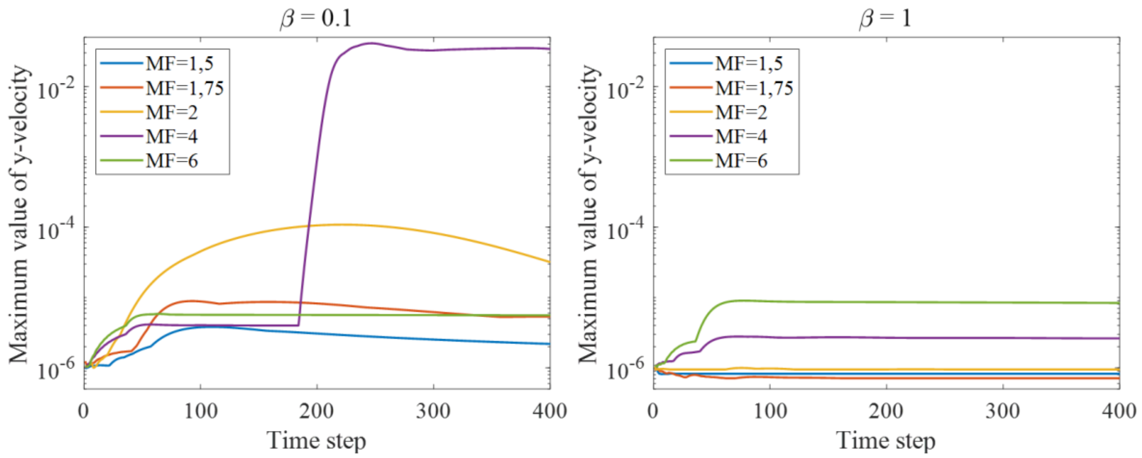

(a) Roe **(b) HLLD**

Figure 8: Time evolutions of the maximum transverse velocities for different values of M_F obtained by the numerical simulations.

4.2 Validation in the parallel shock

The result of the Roe scheme and the HLLD scheme when $M_0 = 20$ and $\beta = 1$ for the parallel shock is shown in Fig.9 as an example. In this condition, both schemes are unstable, which is consistent with Fig.6. However, we found that when β is lower than thresholds for each M_0, both schemes are stable despite the unstable results of the matrix stability analysis. Figure 10 shows the stability maps with HLLD scheme for M_0 versus β, where the stability is determined by whether the transverse velocity increases or decreases in the linear regime. HLLD scheme is always unstable in parallel shocks, which is consistent with the results of the matrix stability analysis.

Figure 11 shows the density contours for the different β with HLLD scheme in parallel shocks. When β is low, the shock thickness becomes broad. The threshold values of β at which the shock thickness becomes broad correspond to the following boundary where the fast magnetosonic Mach number becomes less than unity and the discontinuity ceases to be a fast MHD shock:

$$\beta < \frac{2}{\gamma {M_0}^2}, \tag{12}$$

which is derived from $M_F = u/c_f < 1$ and Eq. (28). Figure 11(a) and (b) correspond to $M_F > 1$ and $M_F < 1$, respectively. For $M_F < 1$, the following relation holds among the fast magnetosonic speed c_f, normal Alfvén speed c_{ax}, sound speed a and flow velocity u in the upstream region of a parallel shock.

$$a < u < c_f = c_{ax}.$$

Then, the left and right signal velocity S_L and S_R are

$$S_L \approx u - c_f < 0, S_R \approx u + c_f > 0.$$

Thus, the Riemann fan extends to both positive and negative side:

$$S_L < 0 < S_R.$$

The numerical viscosity ν_{HLL} of the HLL-type scheme is proportional to the width of the Riemann fan:

$$\nu_{HLL} \propto S_R - S_L,$$

which is large due to the wide Riemann fan compared with that of a super-fast magnetosonic parallel shock when $M_F > 1$, where the sign of the left and right signal velocity is equivalent and the width of the Riemann fan is modest. As a result, the excessive diffusion of HLLD in a sub-fast magnetosonic parallel shock when $M_F < 1$ leads to a thick shock [27].

Figure 12 shows that the density contour at 2,500 time steps and the time evolution of the maximum transverse velocity. The transverse velocity passes through the initial transition region and increases in the linear regime. The slope of the linear regime (≈ 0.005), which can be easily obtained from Fig.12

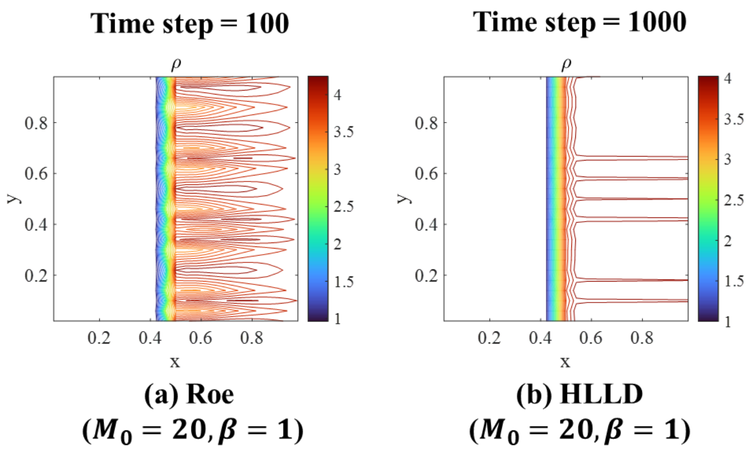

Figure 9: Density contours with Roe and HLLD schemes in parallel shocks: (a) unstable, (b) unstable.

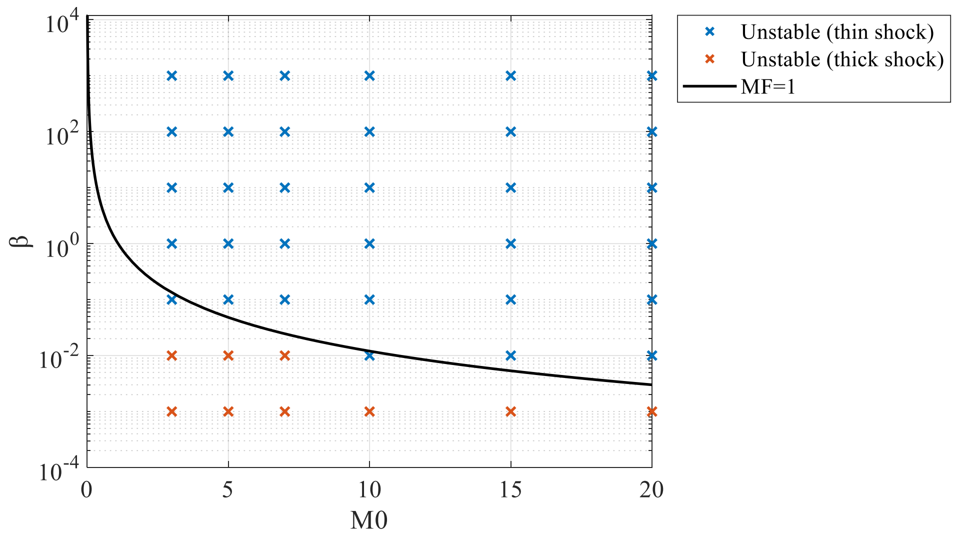

Figure 10: Stability maps with HLLD scheme for M_0 versus β in numerical simulations. Blue crosses indicate unstable thin shock and orange crosses indicate unstable thick shock. The curve of $M_F = 1$ represents Eq. (12), which is the boundary where the shock becomes thick.

is smaller than the maximum value of the real parts of the eigenvalues in the linear analysis ($= 0.008954$) under the same condition. This discrepancy can be attributed to the use of centered approximation to evaluate the numerical flux Jacobian when constructing the stability matrix as mentioned above.

5. Development of the improved HLLD scheme

In the previous sections, we applied the matrix stability analysis originally developed for Euler equations to ideal MHD equations and investigated the carbuncle phenomenon by comparing the linear analysis with numerical simulations. As a result, we found that even widely used HLLD scheme can exhibit the carbuncle instability under certain conditions in MHD simulations. In this section, we propose an improved HLLD scheme that is more robust against the carbuncle instability, and further evaluate the stability of the proposed scheme using the matrix stability analysis.

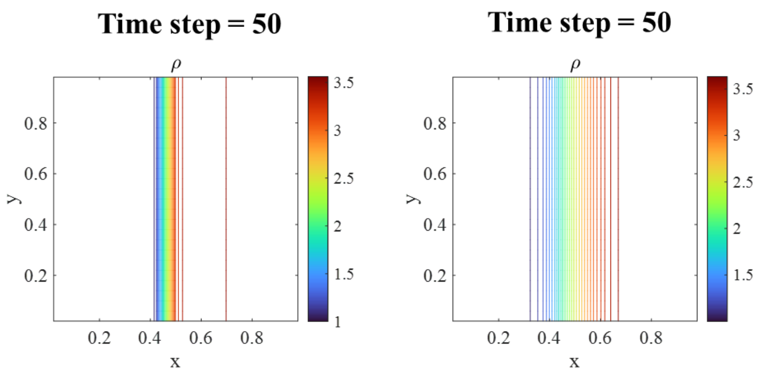

(a) HLLD ($M_0 = 5, \beta = 0.1$)

(b) HLLD ($M_0 = 5, \beta = 0.01$)

Figure 11: Density contours with HLLD scheme in parallel shocks for (a) $M_F > 1$, (b) $M_F < 1$. When $M_F < 1$, the shock becomes thick due to the excessive diffusion.

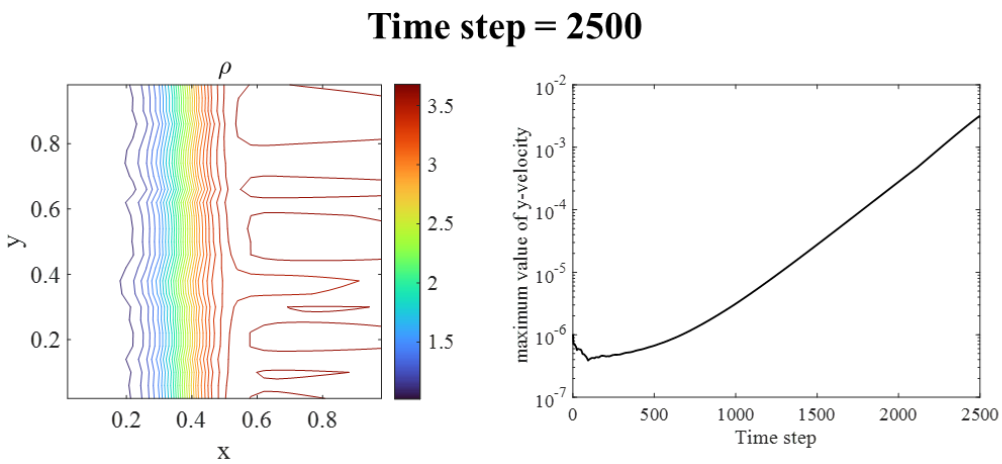

HLLD ($M_0 = 5, \beta = 0.01$)

Figure 12: Density contour at 2,500 time steps and the time evolution of the maximum transverse velocity with HLLD scheme in parallel shocks

5.1 AUSM-like expression of HLLD scheme

In order to develop the robust HLLD scheme, we try to express HLLD scheme in an AUSM-like form. AUSM-family schemes [28] are numerical flux functions known to be simple and robust. In Euler equations, the numerical flux of AUSM-family schemes is split into two parts, advection and pressure parts. In MHD equations, it has been proposed that the numerical flux is split into three parts, namely advection, pressure and magnetic tension parts by Minoshima et al.[22] as follows:

$$\overline{\boldsymbol{F}}_{\boldsymbol{AUSM}} = \frac{\dot{m} + |\dot{m}|}{2}\boldsymbol{\Phi}_{\boldsymbol{L}} + \frac{\dot{m} - |\dot{m}|}{2}\boldsymbol{\Phi}_{\boldsymbol{R}} + \tilde{p}_T\boldsymbol{N} - \boldsymbol{T}, \tag{13}$$

$$\boldsymbol{\Phi} = \left(1, u, v, w, B_y/\rho, B_z/\rho, h\right)^T,$$

$$\boldsymbol{N} = (0,1,0,0,0,0,0\,)^T,$$

$$\boldsymbol{T} = B_x\left(0, B_x/2, B_y, B_z, v, w, \boldsymbol{u_t} \cdot \boldsymbol{B_t}\right)^T,$$

$$\boldsymbol{u_t} = (0, v, w)^T, \boldsymbol{B_t} = (0, B_y, B_z)^T,$$

$$h = \frac{\gamma p}{(\gamma - 1)\rho} + |\boldsymbol{u}|^2 + \frac{|\boldsymbol{B_t}|^2}{\rho},$$

where $\dot{m}, \tilde{p}_T$ and $\boldsymbol{T}$ denote the mass, pressure and magnetic tension fluxes, respectively, at the cell interface in x-direction, and subscripts "L" and "R" signify the left and right states depending on reconstruction methods. Due to this flux splitting, AUSM-family schemes are easily extensible to all-speed and shock-stable scheme.

In order to incorporate this extensibility to HLLD scheme, we propose its AUSM-like expression. First, as for the advection and pressure parts, we employ the AUSM-like expression of HLLC scheme for hydrodynamics proposed by Kitamura et al [21]. Figure 13 shows the Riemann fan of HLLC and HLLD schemes. The Riemann fan of HLLC has two intermediate states separated by two acoustic waves S_L, S_R and an entropy wave S_M, while the Riemann fan of HLLD has four intermediate states separated by two fast waves S_L, S_R, two Alfvén waves S_L^*, S_R^* and an entropy wave S_M. Although HLLC and HLLD have the different intermediate states, density, pressure and normal velocity associated with the advection and pressure fluxes are constant across Alfvén waves. Therefore, the advection and pressure fluxes of HLLD are written as the same formulation as HLLC by replacing the sound speed and gas pressure into the fast magnetosonic speed and total pressure as follows:

$$\overline{\boldsymbol{F}}_{HLLD}^{ADV-PRES} = \frac{\dot{m}+|\dot{m}|}{2}\boldsymbol{\Phi'}_{\boldsymbol{L}} + \frac{\dot{m}-|\dot{m}|}{2}\boldsymbol{\Phi'}_{\boldsymbol{R}} + \tilde{p}_T\boldsymbol{N}, \tag{14}$$

$$\boldsymbol{\Phi'}_{\boldsymbol{L/R}} = \boldsymbol{\Phi}_{\boldsymbol{L/R}} + \left(0,0,0,0,0,0,\frac{\tilde{S}_{L/R}(p_{T*} - p_{T\,L/R})}{\rho_{L/R}(S_{L/R} - u_{L/R})}\right)^T,$$

$$\dot{m} = \begin{cases} \rho_L u_L + \tilde{S}_L(\rho_{L*} - \rho_L), & \text{if } S_* > 0, \\ \rho_R u_R + \tilde{S}_R(\rho_{R*} - \rho_R), & \text{if } S_* \le 0, \end{cases}$$

$$\tilde{p}_T = p_{T*} + \begin{cases} \dfrac{S_*}{S_* - \tilde{S}_L}(p_{T\,L} - p_{T*}), & \text{if } S_* > 0, \\ \dfrac{S_*}{S_* - \tilde{S}_R}(p_{T\,R} - p_{T*}), & \text{if } S_* \le 0, \end{cases}$$

$$\rho_{L/R_*} = \frac{S_{L/R} - u_{L/R}}{S_{L/R} - S_*}\rho_{L/R},$$

$$\tilde{S}_L = \min(0, S_L), \tilde{S}_R = \max(0, S_R),$$

$$S_* = \frac{\alpha_L u_L + \alpha_R u_R - (p_{T\,R} - p_{T\,L})}{\alpha_L + \alpha_R},$$

$$p_{T*} = \frac{1}{2}\{p_{T\,L} + p_{T\,R} + \alpha_L(u_L - S_*) - \alpha_R(u_R - S_*)\},$$

$$p_{T\,L/R} = p_{L/R} + \frac{\left|\boldsymbol{B}_{tL/R}\right|^2}{2},$$

$$\alpha_L = \rho_L(u_L - S_L) > 0, \alpha_R = \rho_R(S_R - u_R) > 0,$$

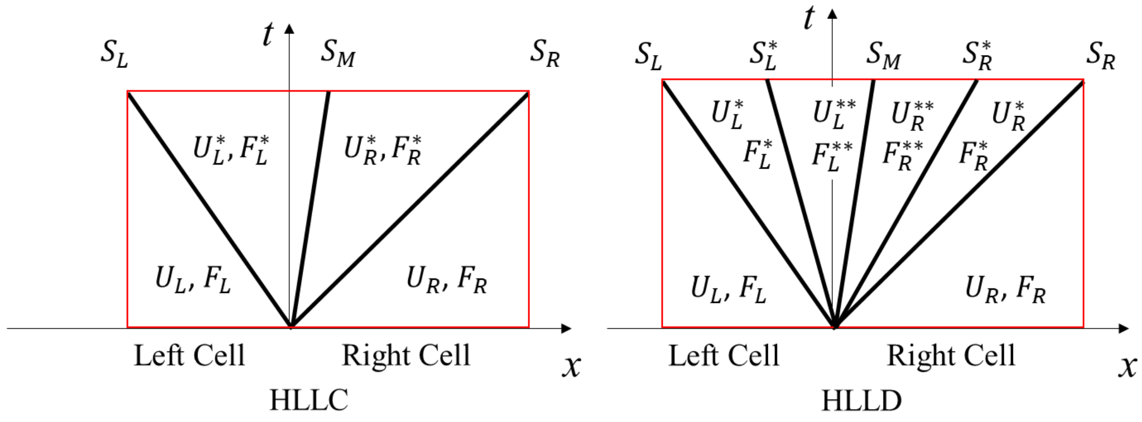

Figure 13: Intermediate states in the Riemann fan of HLLC and HLLD schemes.

where * is referred to as "star region", located between the left and right states as seen in Fig.13. As mentioned above, in HLLD scheme, density, total pressure and normal velocity in "star region" and "double star region" are equivalent. S_L and S_R are the minimum and maximum signal speeds and are written as

$$S_L = \min(u_L, u_R) - \max\left(c_{f_L}, c_{f_R}\right), S_R = \max(u_L, u_R) + \max\left(c_{f_L}, c_{f_R}\right), \tag{15}$$
$$c_f{}^2 = \frac{1}{2}\left[(c_a{}^2 + a^2) + \sqrt{(c_a{}^2 + a^2)^2 - 4a^2 c_{ax}{}^2}\right],$$
$$c_a{}^2 = \frac{|\boldsymbol{B}|^2}{\rho}, c_{ax}{}^2 = \frac{B_x{}^2}{\rho}, a^2 = \gamma\frac{p}{\rho},$$

where c_f, c_a, c_{ax}, a are the fast magnetosonic speed, Alfvén speed, normal Alfvén speed and sound speed, respectively.

Second, as for the magnetic tension part, we employ the magnetic tension flux of a multistate low-dissipation AUSM (MLAU) [22] because it is derived from HLLD and directly applicable to the magnetic tension flux of HLLD. The magnetic tension flux of the tangential momentum is given by

$$(B_x \boldsymbol{B}_t)_{HLLD} = -\dot{m}\{d_L(\boldsymbol{u}_{tL}^* - \boldsymbol{u}_{tL}) + d_R(\boldsymbol{u}_{tR}^* - \boldsymbol{u}_{tR})\} + (A_L^u \boldsymbol{B}_{tL}^* + A_R^u \boldsymbol{B}_{tR}^*) + D^u(\boldsymbol{u}_{tR}^* - \boldsymbol{u}_{tL}^*), \tag{16}$$
$$A_{L/R}^u = sign(B_x)\min\left[|B_x|, \max\left\{0, \frac{\sqrt{\rho_{R/L}^*}(|B_x| \pm \dot{m}/\sqrt{\rho_{R/L}^*})}{\sqrt{\rho_L^*} + \sqrt{\rho_R^*}}\right\}\right],$$
$$D^u = \max\left[0, \frac{\sqrt{\rho_L^*}\sqrt{\rho_R^*}}{\sqrt{\rho_L^*} + \sqrt{\rho_R^*}}\left\{|B_x| - \left(\frac{d_L}{\sqrt{\rho_L^*}} + \frac{d_R}{\sqrt{\rho_R^*}}\right)|\dot{m}|\right\}\right],$$
$$d_L = \frac{1 + sign(\dot{m})}{2}, d_R = \frac{1 - sign(\dot{m})}{2}.$$

Similarly, the magnetic tension flux of the tangential magnetic field is given by

$$(B_x \boldsymbol{u}_t)_{HLLD} = -S_M\{d_L(\boldsymbol{B}_{tL}^* - \widetilde{\boldsymbol{B}}_{tL}) + d_R(\boldsymbol{B}_{tR}^* - \widetilde{\boldsymbol{B}}_{tR})\} + (A_L^B \boldsymbol{u}_{tL}^* + A_R^B \boldsymbol{u}_{tR}^*) + D^B(\boldsymbol{B}_{tR}^* - \boldsymbol{B}_{tL}^*), \tag{17}$$
$$A_{L/R}^B = sign(B_x)\min\left[|B_x|, \max\left\{0, \frac{\sqrt{\rho_{L/R}^*}(|B_x| \pm S_M\sqrt{\rho_{R/L}^*})}{\sqrt{\rho_L^*} + \sqrt{\rho_R^*}}\right\}\right],$$
$$D^B = \frac{D^u}{\sqrt{\rho_L^*}\sqrt{\rho_R^*}},$$

where the tangential components in "star region" are written as

$$\boldsymbol{u}_{tL/R}^* = \boldsymbol{u}_{tL/R} - B_x \frac{S_M - u_{L/R}}{X_{L/R}} \boldsymbol{B}_{tL/R}, \tag{18a}$$
$$\boldsymbol{B}_{tL/R}^* = \widetilde{\boldsymbol{B}}_{tL/R} + B_x^2 \frac{S_M - u_{L/R}}{X_{L/R}(S_{L/R} - S_M)} \boldsymbol{B}_{tL/R}, \tag{18b}$$
$$\widetilde{\boldsymbol{B}}_{tL/R} = \boldsymbol{B}_{tL/R} \frac{S_{L/R} - u_{L/R}}{S_{L/R} - S_M}, \tag{18c}$$
$$X_{L/R} = \rho_{L/R}(S_{L/R} - u_{L/R})(S_{L/R} - S_M) - B_x^2. \tag{18d}$$

Finally, the magnetic tension flux of the total energy is given by

$$(B_x \boldsymbol{u_t} \cdot \boldsymbol{B_t})_{HLLD} = \frac{(B_x \boldsymbol{u}_t)_{HLLD} \cdot (B_x \boldsymbol{B}_t)_{HLLD}}{B_x}. \tag{19}$$

Although Eq. (19) is not an exact form identical to HLLD but a simplified form proposed by Minoshima et al. [22], this approximation is sufficiently accurate for practical use.

To summarize Eq. (16)-(19), the magnetic tension flux is expressed as

$$\overline{\boldsymbol{F}}_{HLLD}^{MT} = -\left(0, B_x^2/2, (B_x B_y)_{HLLD}, (B_x B_z)_{HLLD}, (B_x v)_{HLLD}, (B_x w)_{HLLD}, (B_x \boldsymbol{u_t} \cdot \boldsymbol{B_t})_{HLLD}\right)^T. \tag{20}$$

Consequently, AUSM-like expression of HLLD scheme is as follows:

$$\overline{\boldsymbol{F}}_{\boldsymbol{HLLD}} = \overline{\boldsymbol{F}}_{HLLD}^{ADV-PRES} + \overline{\boldsymbol{F}}_{HLLD}^{MT}. \tag{21}$$

5.2 Improvement of AUSM-like HLLD scheme

In section 5.1, we proposed AUSM-like expression of HLLD scheme by splitting the numerical flux into advection, pressure and magnetic tension parts. As a result of this formulation, we can now apply many ideas that have been proposed so far to improve AUSM-family schemes into HLLD scheme. In the present study, velocity diffusion terms of AUSM+M proposed by Chen et al. [16] are introduced into the pressure flux of AUSM-like HLLD to suppress the carbuncle instability. The velocity diffusion terms of AUSM+M modified for MHD equations are given as

$$p_{ux} = -g\frac{\gamma\left(p_{T_L} + p_{T_R}\right)}{2c_{f_{1/2}}}\psi_L^+\psi_R^-(u_R - u_L), p_{uy} = -g\frac{\gamma\left(p_{T_L} + p_{T_R}\right)}{2c_{f_{1/2}}}\psi_L^+\psi_R^-(v_R - v_L), \tag{22}$$

where ψ_L^+ and ψ_R^- are pressure splitting functions as follows:

$$\psi_{L/R}^{\pm} = \begin{cases} \frac{1}{4}\left(M_{F_{L/R}} \pm 1\right)^2\left(2 \mp M_{F_{L/R}}\right) \pm \frac{3}{16}M_{F_{L/R}}\left(M_{F_{L/R}}^2 - 1\right)^2, & \left|M_{F_{L/R}}\right| < 1 \\ \frac{1}{2}\left(1 \pm sign\left(M_{F_{L/R}}\right)\right), & \left|M_{F_{L/R}}\right| \geq 1 \end{cases}, \tag{23}$$

and g is the pressure-based shock sensing function, which is defined as

$$g = \frac{1 + \cos(\pi h)}{2}, h = \min_k(h_k), h_k = \min\left(\frac{p_{Lk}}{p_{Rk}}, \frac{p_{Rk}}{p_{Lk}}\right), \tag{24}$$

where the subscript k is the index for all adjacent interfaces of both cells in evaluating numerical flux. Here we use gas pressure rather than total pressure because in situations where transverse magnetic field is continuous, for example, when evaluating the y-direction flux in a x-direction parallel shock, the gas pressure difference is absorbed by the continuous magnetic field, reducing the sensitivity of the shock sensor.

Note that, in Eq. (22), the velocity diffusion terms are introduced into the pressure flux not only in the normal direction but also in the transverse direction because it is generally considered that multidimensional effect plays a key role in the carbuncle phenomenon [29, 30].

In [16], the average pressure value is approximated by the combination of the average density value and numerical sound speed as follows:

$$\frac{\gamma(p_L + p_R)}{2a_{1/2}} = \frac{(\rho_L + \rho_R)a_{1/2}}{2}. \tag{25}$$

Even though the above relation does not generally hold in MHD, it is still applied approximately to the present scheme for better robustness.

In addition, in [14, 16], to enhance the resolution of oblique shock and remove the unphysical expansion shock, the numerical sound speed at the interface is given so as to satisfy the Prandtl relation via an oblique shock, while in the present scheme, for simplicity, the numerical fast magnetosonic speed at the interface is given as

$$c_{f_{1/2}} = \begin{cases} c_{f_L}, & S_M > 0 \\ c_{f_R}, & S_M \leq 0 \end{cases}. \tag{26}$$

However, as will be shown in the matrix stability analysis later, this formulation suffers from an instability in low-β parallel shocks. In parallel shocks, the fast magnetosonic speed can be rewritten as the following form from its definition depending on the value of β:

$$c_f = \begin{cases} a, & \beta > 2/\gamma \\ c_{ax}, & \beta \leq 2/\gamma \end{cases}. \tag{27}$$

When $\beta \leq 2/\gamma$, c_f can be rewritten in the following form:

$$c_f = c_{ax} = \frac{B_x}{\sqrt{\rho}} = \sqrt{\frac{2p}{\rho\beta}} = a\sqrt{\frac{2}{\gamma\beta}}. \tag{28}$$

Therefore, from Eq. (22) and (28), the velocity diffusion terms are proportional to the square root of β. On the other hand, as shown in section 4.2, when β becomes even smaller, that is, when Eq. (12) is satisfied, the scheme becomes stable due to the shock thickness. Taking these discussions into account, we modify the fast magnetosonic speed as follows:

$$c_{f\,L/R} = (1-s)\cdot c_{f\,L/R} + s\cdot a_{L/R}, \tag{29}$$

where s is a senser detecting low-β parallel shocks, which is defined as

$$s = H(r_1 - 1)\,exp\left[-\frac{(r_2-1)^2}{\sigma}\right], \tag{30}$$

$$r_1 = \max(\beta_L, \beta_R)\,/\,\min\left(\frac{2}{\gamma M_{0L}^2}, \frac{2}{\gamma M_{0R}^2}\right),$$

$$r_2 = \max\left(\frac{c_{ax}{}_L^2+\varepsilon}{c_{fx}{}_L^2+\varepsilon}, \frac{c_{ax}{}_R^2+\varepsilon}{c_{fx}{}_R^2+\varepsilon}, \frac{c_{ay}{}_L^2+\varepsilon}{c_{fy}{}_L^2+\varepsilon}, \frac{c_{ay}{}_R^2+\varepsilon}{c_{fy}{}_R^2+\varepsilon}\right),$$

$$c_{ax/y} = \frac{B_{x/y}}{\sqrt{\rho}},$$

$$c_{fx/y}{}^2 = \frac{1}{2}\left[(c_a{}^2 + a^2) + \sqrt{(c_a{}^2 + a^2)^2 - 4a^2 c_{ax/y}{}^2}\right],$$

where $H(x)$ denotes a Heaviside step function. The exponential term of senser s is activated when $c_f = c_{ax}\ or\ c_{ay}$ (i.e., $\beta \leq 2/\gamma$). The Heaviside step function is introduced to switch off the senser for $\beta < 2/\gamma {M_0}^2$, since activation when $\beta < 2/\gamma {M_0}^2$ causes the numerical breakdown. This is because when $\beta > 2/\gamma {M_0}^2$, in which case $u > c_f$, the correction of c_f has little influence on the wave speeds S_L and S_R. However, when $\beta < 2/\gamma {M_0}^2$, in which case $u < c_f$, the correction of c_f results in an underestimation of the wave speeds. Here, defining the numerator as the maximum value and the denominator as the minimum value in r_1, and activating the switch when $r_1 > 1$ introduces a relaxation in the switching criterion. This allows the wave speeds to be adjusted to a level that prevents numerical breakdown even when the fast magnetosonic Mach number slightly falls below unity, thereby reducing shock thickness. The value of σ is chosen as 10^{-6} through numerical experiments.

Finally, the improved HLLD flux can be accomplished by adding Eq. (22) into Eq. (21) and modifying the fast magnetosonic speed as shown in Eq. (29) as follows:

$$\overline{\boldsymbol{F}}_{HLLD\_present} = \overline{\boldsymbol{F}}_{HLLD}^{ADV-PRES} + \overline{\boldsymbol{F}}_{HLLD}^{MT} + \left(0, p_{ux}, p_{uy}, 0,0,0,0\right)^T. \tag{31}$$

We call the proposed scheme HLLD+M and the stability of this scheme will be analyzed in the next section.

5.3 Matrix stability analysis of the proposed scheme

We investigate the stability of the proposed scheme HLLD+M by the matrix stability analysis. First, the stability for the perpendicular shock is shown in Fig.14, where the results of MLAU [22] and Low-dissipation HLLD (LHLLD) [23], proposed as robust MHD schemes, are also presented for comparison. Figure 14 indicates that HLLD+M is stable for a wide range of M_F, while MLAU and LHLLD are only slightly more stable compared with HLLD, as shown in Fig.5(b).

Second, the stability for the parallel shock is shown in Fig.15, where the results with and without the modification of the numerical fast magnetosonic speed at the interface (Eq. (29)) are presented to examine the effect of the modification. Indeed, without the modification, in the high-β regime ($\beta > 2/\gamma$), the stability is improved compared with HLLD, while in the moderate- and low-β regime ($\beta < 2/\gamma$), the scheme remains unstable. On the other hand, with the modification, the stability in the moderate-β regime ($2/\gamma {M_0}^2 < \beta < 2/\gamma$) is improved without degrading the stability in the high-β regime. Although in the low-β regime ($\beta < 2/\gamma {M_0}^2$) the stability is not improved, this is the effect of the Heaviside step function in Eq. (30), which is necessary to prevent the numerical breakdown.

These results demonstrate that HLLD+M significantly improves the stability compared with the original HLLD and other schemes known as robust for MHD equations.

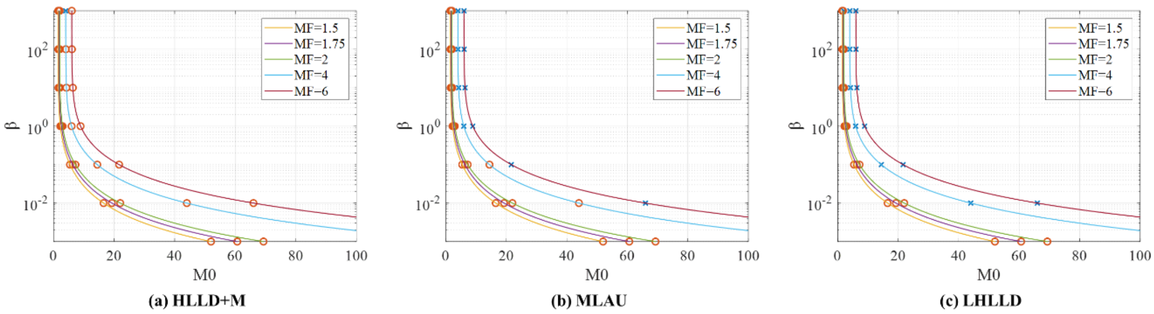

Figure 14: Stability maps for M_0 versus β on the curves where M_F is constant for (a) HLLD+M, (b) MLAU and (c) LHLLD.

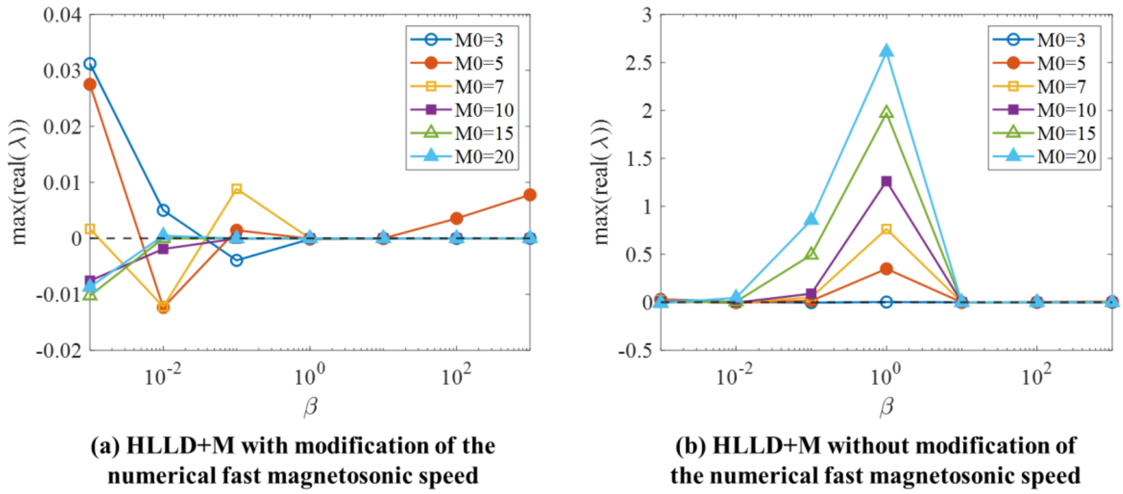

Figure 15: Maximum values of the real parts of the eigenvalues against β for each M_0 for HLLD+M (a) with and (b) without modification of the numerical fast magnetosonic speed (Eq. (29)) in parallel shocks.

6. Numerical tests

This section presents the numerical simulation results of MHD test problems to assess the capability of HLLD+M scheme through comparison with the HLLD, MLAU and LHLLD schemes. We employ the second order MUSCL reconstruction with a minmod limiter for spatial reconstruction, the third order TVD Runge–Kutta method [31] for time integration, and hyperbolic divergence cleaning method [26] to constrain the divergence error. The specific heat ratio γ is 5/3 and CFL number is 0.4, unless otherwise stated.

6.1 Parallel shock

This test is the same situation as that of section 4.2, where Roe and HLLD scheme are unstable for $M_F > 1$. The results of HLLD+M scheme when β is high, moderate and low at $M_0 = 20$ at 1,000 time steps are shown in Fig.16. There are no signs of carbuncle or other shock anomalies observed in Fig.9. These results agree well with the matrix stability analysis in Fig.15. Moreover, it is observed that for $\beta = 0.001$, the shock thickness is slightly reduced by the correction of c_f as mentioned in section 5.2. As shown in Fig.16(d), when r_1 in Eq. (30) is altered to $r_1 = \min(\beta_L, \beta_R) / \max(2/\gamma M_{0L}^2, 2/\gamma M_{0R}^2)$, the shock becomes thicker than that in Fig.16(c). However, for $\beta = 0.001$, as mentioned in section 4.2, the transverse velocity slowly grows, leading to the instability after a large number of time steps more than 2,000 time steps like HLLD. An improvement of the stability for the low-β parallel shocks is left for future work.

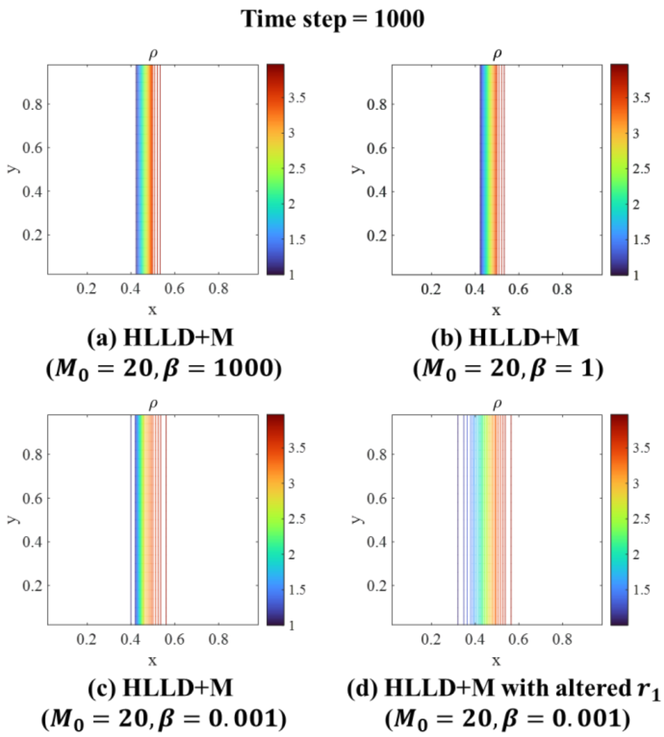

Figure 16: Density contours of HLLD+M scheme in parallel shocks for (a) high-β $(2/\gamma < \beta)$, (b) moderate-β $(2/\gamma M_0^2 < \beta < 2/\gamma)$, (c) low-$\beta$ $(\beta < 2/\gamma M_0^2)$ and (d) low-β $(\beta < 2/\gamma M_0^2)$ with altered r_1.

6.2 Orszag-Tang vortex

The Orszag–Tang vortex is a standard two-dimensional MHD test problem to verify the capability of capturing multiple interactions of shock waves and vortices [32]. The initial condition is

$$(\rho, u, v, w, B_x, B_y, B_z, p) = (\gamma^2, -\sin(y), \sin(x), 0, -\sin(y), \sin(2x), \gamma).$$

The computational domain of $0 < x < 2\pi$ and $0 < y < 2\pi$ is resolved by 100×100 cells. The computations are conducted until $t = \pi$. The periodic boundary condition is applied to all the boundaries.

In Fig.17, the density contours are shown for HLLD and HLLD+M. They overall look similar, capturing important physics such as shock interactions. The density profiles along $y = 1$ line are shown in Fig.18. This result also indicates that HLLD and HLLD+M have almost the same profile. From this example, it is demonstrated that HLLD+M successfully handle complex shock interactions as well as HLLD despite the additional diffusion term.

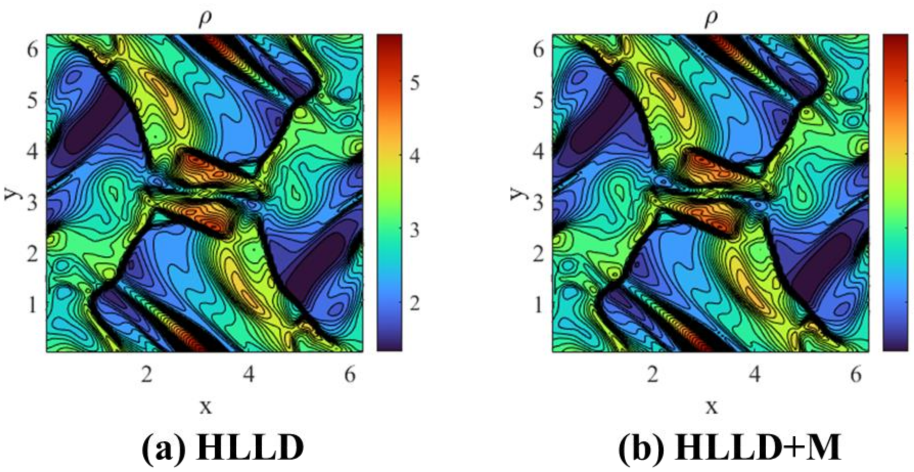

Figure 17: Density contours in the Orszag–Tang vortex with (a) HLLD and (b)HLLD+M.

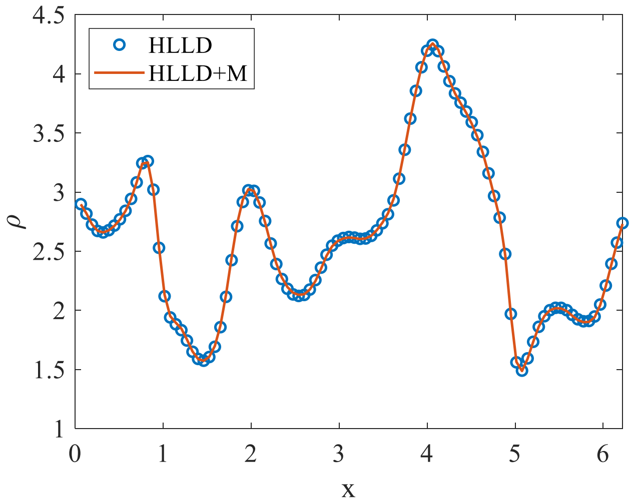

Figure 18: Density profiles along $y = 1$ line in the Orszag–Tang vortex with HLLD and HLLD+M.

6.3 MHD blast wave

In this test problem, we simulate the propagation of MHD shock in a strongly magnetized medium. There are several variants for this problem, but we set the initial condition as follows [33]:
$(\rho, u, v, w, B_x, B_y, B_z, p) = (1,0,0,0,10/\sqrt{2}, 10/\sqrt{2}, 0,100)$, inside a circle centered at the origin with 0.125 radius,
$(\rho, u, v, w, B_x, B_y, B_z, p) = (1,0,0,0,10/\sqrt{2}, 10/\sqrt{2}, 0,1)$, elsewhere.
The computational domain of $-0.5 < x < 0.5$ and $-0.5 < y < 0.5$ is resolved by 256×256 cells. The computations are conducted until $t = 0.02$.

The density contours and profiles along $x + y = 0$ line are shown in Fig.19 and Fig.20, respectively, for HLLD and HLLD+M. From these figures, almost no noticeable difference can be observed. This indicates that although β is low (= computationally severe setup) in the low-pressure region ($\beta = 0.02$) in this test problem, the senser in Eq. (30) is not activated unless the shock is a parallel shock and an appropriate amount of dissipation is provided.

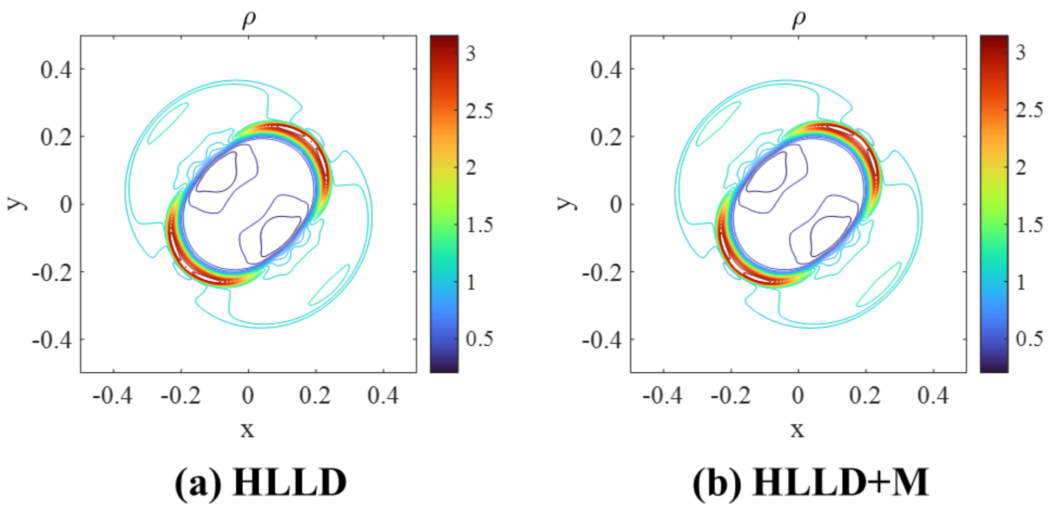

Figure 19: Density contours in the MHD Blast Wave with (a) HLLD and (b)HLLD+M.

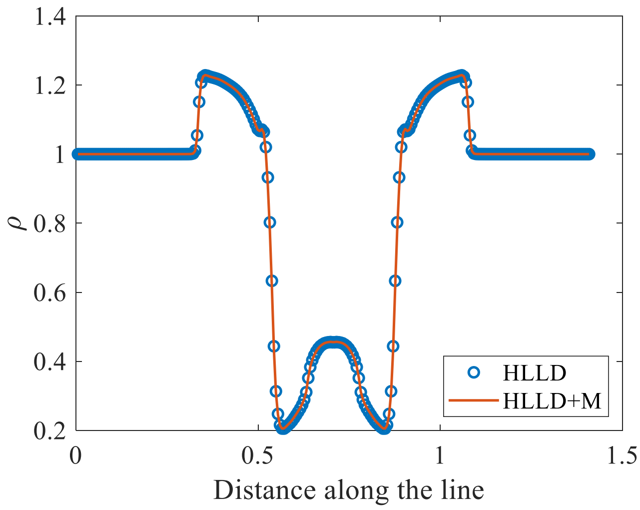

Figure 20: Density profiles along $x + y = 0$ line in the MHD Blast Wave with HLLD and HLLD+M.

6.4 MHD rotor

In this test problem, we simulate the strong torsional Alfvén waves, which are generated by the rapid rotation of the dense fluid and launched into the surrounding medium. We set the initial condition as follows [34]:

$$\boldsymbol{B} = \left(\frac{2.5}{\sqrt{4\pi}}, 0,0\right), p = 1, w = 0,$$

$$(\rho, u, v) = \begin{cases} (10, u_r, v_r), & r \leq 0.1 \\ (1 + 9f_r, u_r f_r, v_r f_r), & 0.1 < r \leq 0.115, \\ (1,0,0), & 0.115 < r \end{cases}$$

with $u_r = 5 - 10y, v_r = 10x - 5, f_r = (23 - 200r)/3$ and $r = \sqrt{(x - 0.5)^2 + (y - 0.5)^2}$. The computational domain of $0 < x < 1$ and $0 < y < 1$ is composed of 400×400 cells. The periodic boundary condition is applied to all the boundaries. The computations are conducted until $t = 0.25$.

The pressure contours and profiles along $y = x$ line are shown in Fig.21 and Fig.22, respectively, for HLLD and HLLD+M. From these figures, almost no noticeable difference can be observed. This indicates that the additional diffusion term of the pressure flux does not affect the resolution of the Alfvén waves.

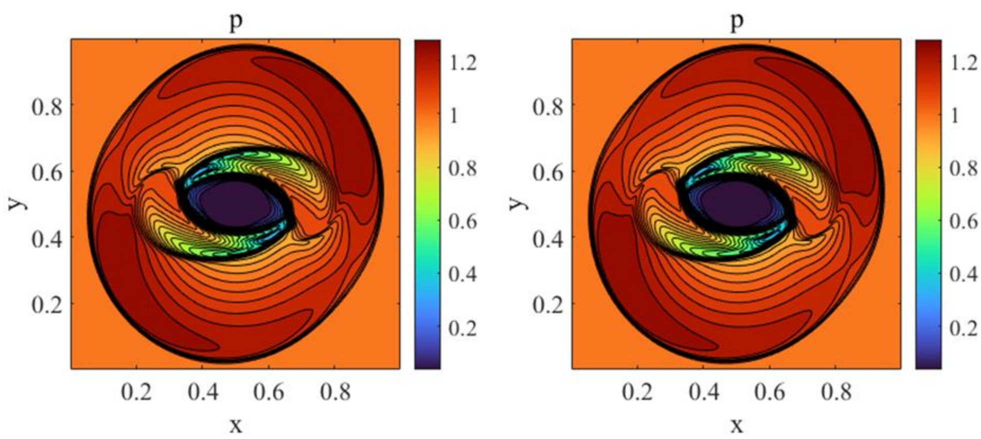

(a) HLLD **(b) HLLD+M**

Figure 21: Pressure contours in the MHD Rotor with (a) HLLD and (b) HLLD+M.

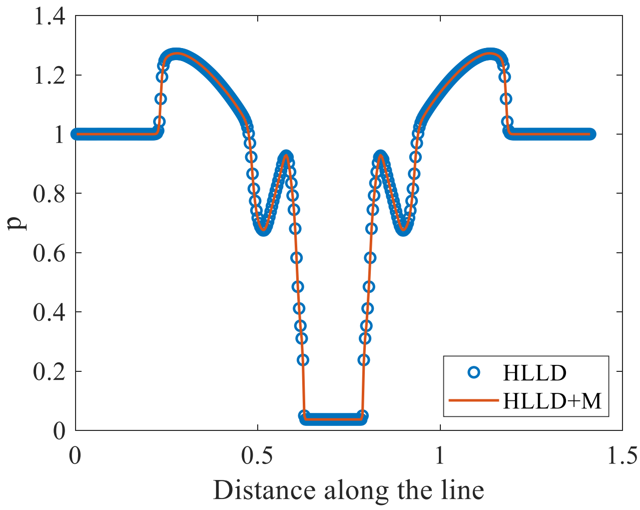

Figure 22: Pressure profiles along $y = x$ line in the MHD Rotor with HLLD and HLLD+M.

6.5 Richtmyer-Meshkov instability

We simulate the Richtmyer-Meshkov instability induced when a shock collides with a corrugated contact discontinuity. The initial condition is as follows [22, 23]:

$$(\rho, u, v, w, B_x, B_y, B_z, p) = (1, 0, -1, 0, 0.000034641, 0, 0, 0.00006), \qquad y > 0,$$

$$(\rho, u, v, w, B_x, B_y, B_z, p) = (3.9988, 0, -0.250075, 0, 0.000138523, 0, 0, 0.75), \qquad y < 0,$$

which satisfies the Rankine-Hugoniot condition for perpendicular shocks. The upstream Mach number is $M_0 = 100$ and the plasma beta is $\beta = 10^5$. A corrugated contact discontinuity is located in the upstream region, $y_{cd} = Y_0 + \psi_0 \cos(2\pi x/\lambda)$, where $Y_0 = 1$, $\psi_0 = 0.1$ is the corrugation amplitude,

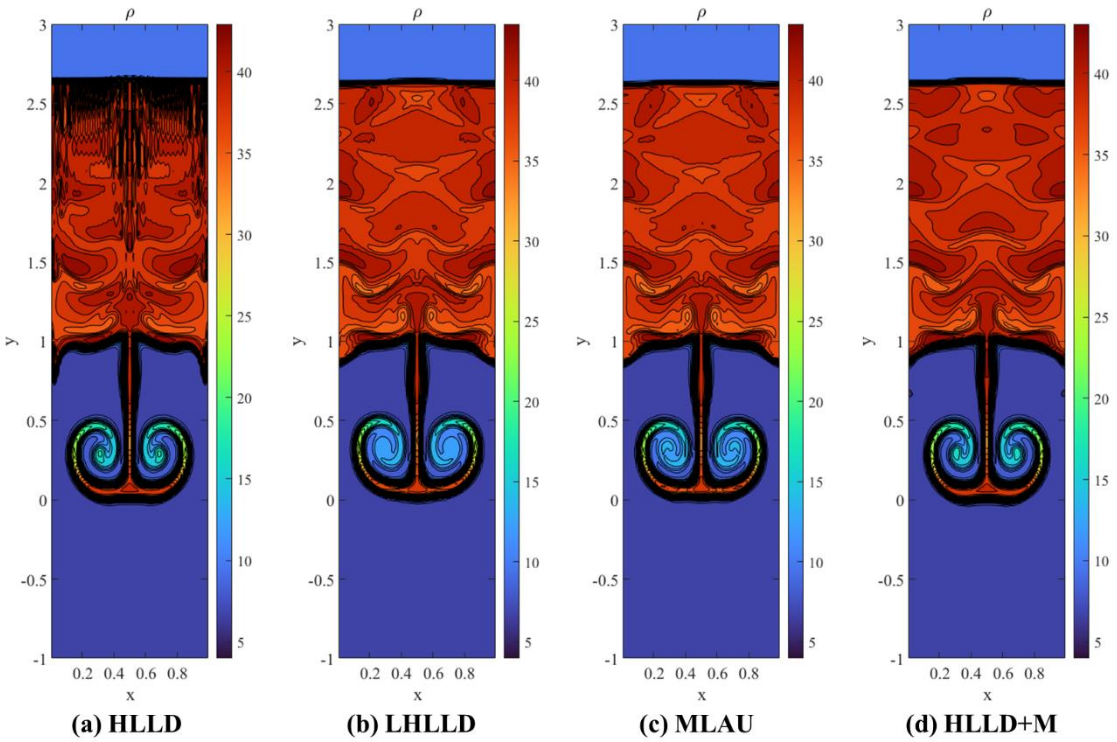

Figure 23: Density contours in the Richtmyer-Meshkov instability with (a) HLLD, (b) LHLLD, (c) MLAU and (d) HLLD+M.

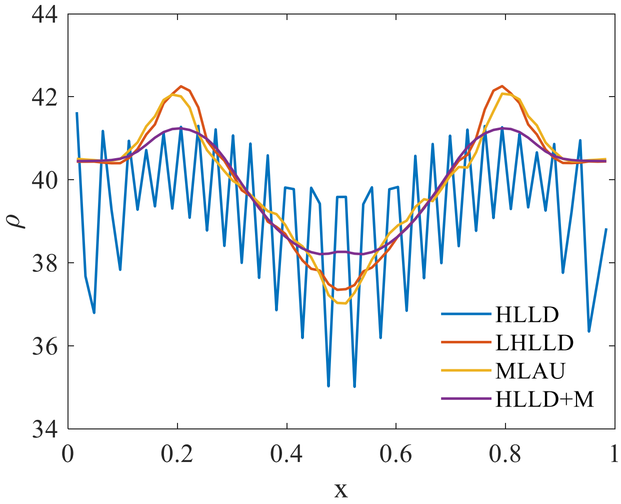

Figure 24: Density profiles along $y = 2.5$ line in the Richtmyer-Meshkov instability with HLLD, LHLLD, MLAU and HLLD+M.

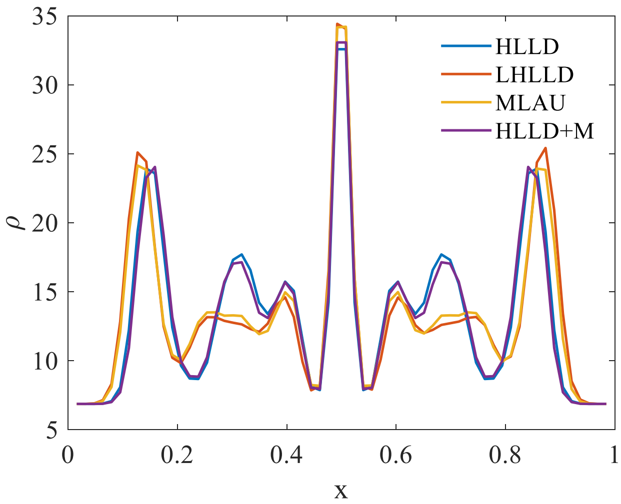

Figure 25: Density profiles along $y = 0.3$ line in the Richtmyer-Meshkov instability with HLLD, LHLLD, MLAU and HLLD+M.

and $\lambda = 1.0$ is the wavelength. The density behind the contact discontinuity $y > y_{cd}$ is given by $\rho = 10$. We shift a frame moving with $v = -0.625$, which is the interface velocity after the collision with the incident shock so that the structure of the RMI stays around $y = 0$ during the simulation, leading to minimization of the numerical dissipation for capturing the contact discontinuity. The computational domain of $-\lambda/2 < x < \lambda/2$ and $-20\lambda < y < 20\lambda$ is composed of $N \times 40N$ cells ($\Delta y/\Delta x = 1$), where $N = 64$. The boundary condition is periodic in the x-direction and is fixed to the initial state in the y-direction. CFL number is set to 0.4.

Figure 23 shows the density contours at $t = 15$ obtained with (a) HLLD, (b) LHLLD, (c) MLAU and (d) HLLD+M scheme. HLLD scheme exhibits the grid-scale oscillation at the shock front, while the other schemes successfully eliminate this unphysical oscillation as shown in Fig.24. Figure 25 indicates that the profiles of HLLD and HLLD+M are similar and the additional diffusion term of the pressure flux does not degrade the accuracy of the spike, while the profiles of LHLLD and MLAU are smeared.

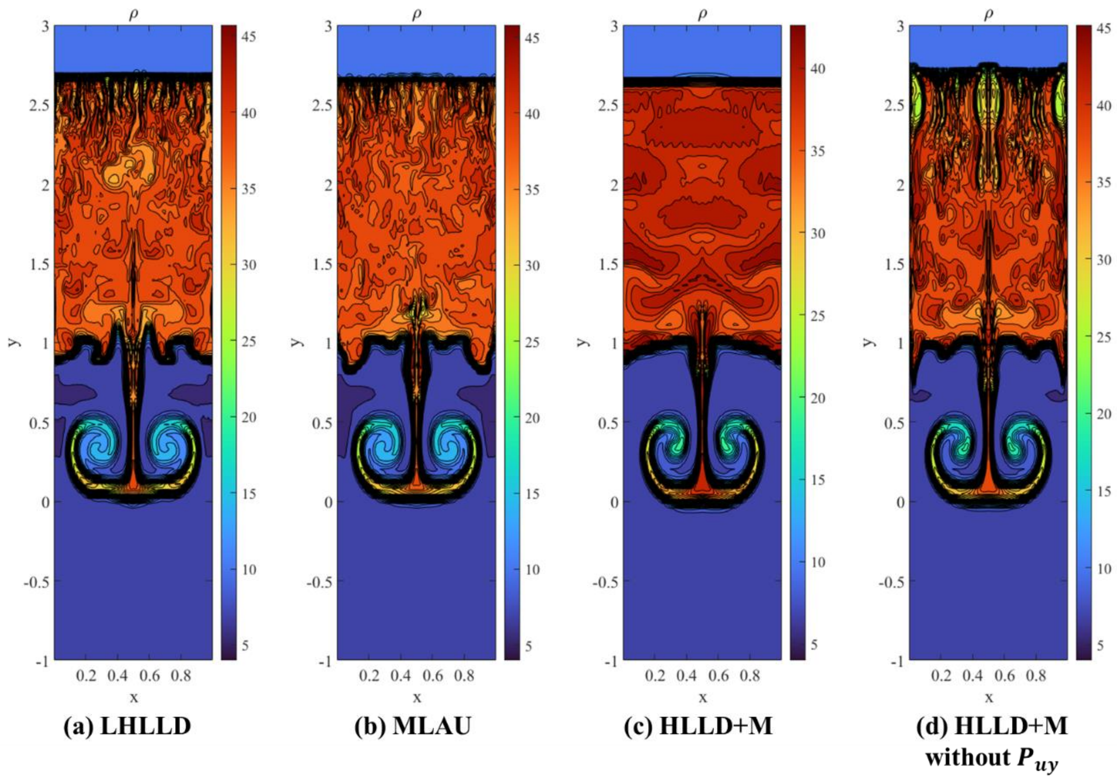

Figure 26: Density contours in the Richtmyer-Meshkov instability with (a) LHLLD, (b) MLAU, (c) HLLD+M and (d) HLLD+M without P_{uy}.

Under a more stringent condition, where the grid aspect ratio is set to $\Delta y/\Delta x = 4$ with a $2N \times 40N/2$ grid resolution, the density contours at $t = 15$ obtained with (a) LHLLD, (b) MLAU, (c) HLLD+M and (d) HLLD+M without p_{uy} in Eq. (22) are presented in Fig.26. It is observed that only HLLD+M suppresses the unphysical oscillation for this severe test, and the transverse diffusion term p_{uy} is found effective for stabilizing shocks aligned with high-aspect-ratio grids. It is thought that the transverse dissipation suppresses the transverse perturbations that are believed to trigger the carbuncle phenomenon. It is confirmed that HLLD+M is more robust against shock anomalies than the other existing schemes within the scope of the present tests.

7. Conclusions

In this study, we applied the matrix stability analysis of the carbuncle phenomenon, which has been validated in Euler equations, to ideal MHD equations for the first time. First, the results of the matrix stability analysis for perpendicular shocks showed that HLL scheme is stable for any M_0 and β, while the stability of Roe and HLLD schemes depends on the relationship between M_0 and β. Moreover, the results suggested the existence of a critical fast magnetosonic Mach number at which the shock becomes unstable. This insight was validated through the numerical simulations by focusing on the evolution of the transverse velocity.

Second, the results of the matrix stability analysis for parallel shocks showed that HLL scheme is stable for any M_0 and β, while the stability of Roe and HLLD schemes are unstable for any upstream Mach number M_0 and plasma-beta β, which is consistent with the results of the matrix stability analysis.

We expressed HLLD scheme in an AUSM-like form and improved the shock robustness by adding the velocity diffusion term into the pressure flux, as inspired from AUSM+M for hydrodynamics, leading to HLLD+M scheme. In particular, the numerical fast magnetosonic speed varying with β was introduced for the robustness against the parallel shocks. The results of the matrix stability analysis indicated that the present scheme is stable for a wide range of the fast magnetosonic Mach number in perpendicular shocks in MHD. Also, in parallel shocks, the stability is improved except for the low-β regime.

The numerical tests demonstrated that the proposed scheme produced almost identical results to HLLD for basic MHD test problems. This showed that the additional diffusion term has no adverse effect on the accuracy of the solution. In the Richtmyer-Meshkov instability, the shock robustness of the present scheme was compared with the HLLD, LHLLD and MLAU schemes. These results indicated that the present scheme is more robust than the other schemes even in the high-aspect-ratio grids.

This study provides insights into the mechanisms underlying numerical shock instabilities in magnetohydrodynamics and lays the foundation for further investigations of this phenomenon. In particular, parallel shocks under low-β conditions require further investigation. The remaining challenges are the all-speed extension of the present scheme and the enhancement of stability in low-β plasmas. The AUSM-like expression of HLLD will contribute to improving the extensibility for these challenges.

Acknowledgements

This work was supported by JSPS KAKENHI Grant Number JP26K01133, and Suzuki Foundation.

References

[1] K. M. Peery, S. T. Imlay, Blunt body flow simulations, AIAA Paper 88-2924, 1988.

[2] J. Quirk, A contribution to the great Riemann solver debate, Int. J. Numer. Methods Fluids., 18, 555-574, 1994.

[3] M. Pandolfi, D. D'Ambrosio, Numerical instabilities in upwind methods: analysis and cures for the "carbuncle" phenomenon, J. Comput. Phys., 166(2), 271-301, 2001.

[4] Y. Chauvat, J. M. Moschetta, and J. Gressier, Shock Wave Numerical Structure and the Carbuncle Phenomenon, International Journal for Numerical Methods in Fluids, Vol. 47, Nos. 8–9, 903–909, 2005.

[5] K. Kitamura, P. L. Roe, and F. Ismail, Evaluation of Euler Fluxes for Hypersonic Flow Computations, AIAA Journal, Vol. 47, No. 1, 44–53, 2009.

[6] T. Miyoshi, K. Kusano, A robust MHD scheme in space weather modeling: a carbuncle-free HLL-type solver, AGU Fall Meeting, SM41A-0311, 2007

[7] T. Hanawa, H. Mikami, T. Matsumoto, Improving shock irregularities based on the characteristics of the MHD equations, J. Comput. Phys., 227, 7952-7976, 2008.

[8] M. Dumbser, J. M. Moschetta, J. Gressier, A matrix stability analysis of the carbuncle phenomenon, J. Comput. Phys., 197, 647-670, 2004.

[9] Z. Chen, X. Huang, Y. X. Ren, Z. Xie, and Ming Zhou, Mechanism Study of Shock Instability in Riemann-Solver-Based Shock-Capturing Scheme, AIAA Journal, Vol. 56, No. 9, 3636-3651, 2018.

[10] Z. Chen, X. Huang, Y. X. Ren, Z. Xie, and Ming Zhou, Mechanism-Derived Shock Instability Elimination for Riemann-Solver-Based Shock-Capturing Scheme, AIAA Journal, Vol. 56, No. 9, 3652-3666, 2018.

[11] Y. Wada, M.-S. Liou, An accurate and robust flux splitting scheme for shock and contact discontinuities, SIAM Journal of Scientific Computation, 18 (3), 633–657, 1997.

[12] M.-S. Liou, A sequal to AUSM: AUSM + , J. Comput. Phys., 129, 364–382, 1996.

[13] M.-S. Liou, A sequel to AUSM, part II: AUSM + -up for all speeds, J. Comput. Phys., 214, 137–170, 2006.

[14] K.H. Kim, C. Kim, O.H. Rho, Methods for the accurate computations of hypersonic flows I: AUSMPW + scheme, J. Comput. Phys., 174, 38–80, 2001.

[15] K. Kitamura, E. Shima, Towards shock-stable and accurate hypersonic heating computations: a new pressure flux for AUSM-family schemes, J. Comput. Phys., 245, 62–83, 2013.

[16] S.-S. Chen, F.-J. Cai, H.-C. Xue, N. Wang, and C. Yan, An improved AUSM-family scheme with robustness and accuracy for all Mach number flows, Applied Math. Modeling, 77, 1065-1081, 2020.

[17] A.K. Pandare and J.R. Edwards, Stable low diffusion flux splittng schemes on unstructured meshes, J. Comput. Phys., 543, 114415, 2025.

[18] A. Harten, P. Lax, and B. van Leer, On upstream differencing and Godunov-type schemes for hyperbolic conservation laws, SIAM Rev, 25(1), 35-61, 1983.

[19] E.F. Toro, M. Spruce, W. Speares, Restoration of the contact surface in the HLL-Riemann solver, Shock Waves, 4, 25–34, 1994.

[20] M.-S. Liou, Mass flux schemes and connection to shock instability, J. Comput. Phys., 160, 623–648, 2000.

[21] K. Kitamura and E. Shima, AUSM-like expression of HLLC and its all-speed extension, Int Numer Meth Fluids, 92, 246-2265, 2020.

[22] T. Minoshima, K. Kitamura, T. Miyoshi, A multistate low-dissipation advection upstream splitting method for ideal magnetohydrodynamics, Astrophys. J. Suppl. Ser., 248, 12, 2020.

[23] T. Minoshima, T. Miyoshi, A low-dissipation HLLD approximate Riemann solver for a very wide range of Mach numbers, J. Comput. Phys., 446, 110639, 2021.

[24] T. Miyoshi, K. Kusano, A multi-state HLL approximate Riemann solver for ideal magnetohydrodynamics, J. Comput. Phys., 208, 315–344, 2005.

[25] M. Brio, and C. C. Wu, An upwind differencing scheme for the equations of ideal magnetohydrodynamics, J. Comput. Phys., 75, 400-422, 1988

[26] A. Dedner, F. Kemm, D. Kroner, C-D. Munz, T. Schnitzer, M. Wesenberg, Hyperbolic

divergence cleaning for the MHD equations, J. Comput. Phys., 175, 645–73, 2002.

[27] S. Jin and J.-G. Liu, The effects of numerical viscosities: I. Slowly moving shocks, J. Comput. Phys 126, 373–389, 1996.

[28] M.-S. Liou, C.J. Steen, A new flux splitting scheme, J. Comput. Phys., 107, 23–39, 1993.

[29] J.-M. Moschetta, J. Gressier, J.-C. Robinet, G. Casalis, The carbuncle phenomenon: a genuine Euler instability ?, in: E.F. Toro (Ed.) Godunov Methods, Theory and Applications, Kluwer Academic/Plenum Publishers, 639–645, 1995.

[30] S.-S. Chen, C. Yan, B.-X. Lin, L.-Y. Liu, J. Yu, Affordable shock-stable item for Godunov-type schemes against carbuncle phenomenon, J. Comput. Phys., 373, 662–672, 2018.

[31] C. Shu, S. Osher, Efficient implementation of essentially non-oscillatory shock-capturing schemes, J. Comput. Phys., 77, 439, 1988.

[32] S. A. Orszag and C. M. Tang, Small-Scale Structure of Two-Dimensional Magnetohydrodynamic Turbulence, Journal of Fluid Mechanics, 90, 129–143, 1979.

[33] K. Kitamura, T. Mamashita, D. Ryu, SLAU2 applied to two-dimensional, ideal magnetohydrodynamics simulations, Computers & Fluids, 209, 104635, 2020.

[34] R. Dematté, A. A. Farmakalides, S. Millmore, N. Nikiforakis, An all Mach number scheme for visco-resistive magnetically-dominated MHD flows, J. Comput. Phys., 514, 113229, 2024.

[35] J. P. Goedbloed, Time reversal duality of magnetohydrodynamic shocks, Physics of Plasmas, 15, 062101, 2008.